Nanoscale Advances

ROYAL SOCIETY OF CHEMISTRY

PAPER

View Article Online
View Journal | View Issue

Cite this: *Nanoscale Adv.*, 2024, **6**, 126

High-throughput large scale microfluidic assembly of iron oxide nanoflowers@PS-*b*-PAA polymeric micelles as multimodal nanoplatforms for photothermia and magnetic imaging†

Emilia Benassai, [a] Ana C. Hortelao,[a] Elif Aygun,[bc] Asli Alpman, [bc] Claire Wilhelm,[d] Emine Ulku Saritas [bc] and Ali Abou-Hassan *[ae]

Received 29th August 2023
Accepted 17th November 2023

DOI: 10.1039/d3na00700f

rsc.li/nanoscale-advances

Magnetic nanoparticles have been extensively explored as theranostic agents both in academic and clinical settings. Their self-assembly into nanohybrids using block copolymers can lead to new nanostructures with high functionalities and performances. Herein, we demonstrate a high-throughput and scalable method to elaborate magnetic micelles by the assembly of iron oxide magnetite nanoflowers, an efficient nanoheater, and the block copolymer Poly(styrene)-*block*-poly(acrylic acid) *via* a microfluidic-assisted nanoprecipitation method. We show that the size and shape of the magnetomicelles can be easily tuned by modulating the residence time in the microfluidic channel. In addition to their biocompatibility, we demonstrate the potential of these magnetic nanohybrids as multimodal theranostic platforms capable of generating heat by photothermia and functioning as negative contrast agents in magnetic resonance imaging and as imaging tracers in magnetic particle imaging. Notably, they outperform currently commercially available particles in terms of imaging functionalities.

Introduction

Iron oxide nanoparticles (NPs) are outstanding candidates in the field of biomedical applications due to their superparamagnetic properties and biocompatibility.[1–3] They are used as multimodal theranostic agents in nanomedicine, such as in magnetic resonance imaging (MRI), or more recently magnetic particle imaging (MPI), drug delivery, magnetic hyperthermia, magnetic targeting and manipulation.[4–9] In addition to such a panel of functionalities, the possibility to use magnetic nanoparticles as hot spots for heat generation under light stimulation by photothermia (PT) was demonstrated recently adding to the realm of therapeutic modalities of these NPs.[10–14] Among these efficient magnetic nanoparticles photothermally competent, polyol synthesized magnetite iron oxide nanoflowers (IONFs), have shown excellent photothermal conversion when excited in the therapeutic near infrared biological windows which were maintained *in cellulo*.[12,15,16]

Polymers are extremely diverse materials that can assemble in a variety of different shapes with acceptable sizes for biomedical applications.[17] In particular, block copolymers (BCPs) are gaining increasing attention as nanocarriers as they are formed by more than two different polymeric moieties, each one presenting very peculiar physicochemical properties.[18,19] The most used block copolymers are made of one, or more, hydrophilic moiety and one, or more, hydrophobic moiety and the resulting molecules possess a mixed nature with interesting solubility (amphiphilic) features. Assembly of preformed inorganic NPs and BCPs is a great strategy for the elaboration of multifunctional nanohybrids of different hierarchical structures and length scales with high performances and functionalities.[20–22]

Poly(styrene)-*block*-poly(acrylic acid) (PS-PAA) is one of the most frequently studied BCPs.[23] It has been proposed in numerous examples for drug delivery purposes in different forms mostly in the micelle one.[24–26] PS-*b*-PAA micelle formation thermodynamics and kinetics were fully studied and described by Adi Eisenberg and co-workers, as well as the influence of many parameters over their shape control in bulk syntheses.[17]

[a]*Sorbonne Université, PHysico-chimie des Électrolytes et Nanosystèmes InterfaciauX (PHENIX), UMR CNRS 8234, F-75005, Paris, France. E-mail: ali.abou_hassan@sorbonne-universite.fr*

[b]*Department of Electrical and Electronics Engineering, Bilkent University, Ankara 06800, Turkey*

[c]*National Magnetic Resonance Research Center (UMRAM), Bilkent University, Ankara 06800, Turkey*

[d]*Laboratoire Physico Chimie Curie, PCC, Institut Curie, Sorbonne University, PSL University, CNRS UMR168, Paris 75005, France*

[e]*Institut Universitaire de France (IUF), 75231 Cedex 05, Paris, France*

† Electronic supplementary information (ESI) available: Experimental conditions for the synthesis of magnetomicelles, size distribution histograms, dynamic light scattering characterizations, UV-Vis-NIR spectra, Beer–Lambert plot, real and imaginary data for Mie scattering calculations, simulated cross sections and aggregation parameter measurements. See DOI: https://doi.org/10.1039/d3na00700f

Considering the remarkable magnetic and optical properties of IONFs and the useful role of block copolymers, one might consider combining both functionalities in a hybrid nanocomposite. Hybrid nanocomposites are usually obtained in bulk solution by self-assembly using the modified co-solvent protocol: hydrophobic nanoparticles such as oleate-modified iron oxide NPs are added to the solution of polymer in an aprotic solvent like tetrahydrofuran (THF) and water is gradually added.[27] Iron oxide NPs spontaneously assemble and localize in the micellar hydrophobic core by hydrophobic interactions. In literature, the self-assembly of magnetic NPs and PS-*b*-PAA BCP has been used as a strategy for formulation of nanohybrids with different spatial organizations. Kim *et al.*[27] used a co-solvent method to efficiently encapsulate maghemite γ-Fe_2O_3 nanoparticles into PS_{250}-*p*-PAA_{13} micelles, and, Hickey *et al.*[28] studied the assembly of PS-*b*-PAA under different batch synthesis conditions. Nonetheless, the literature is still scarce regarding the specific production of PS-*b*-PAA magnetomicelles and the characterization of their functionalities in the frame of biomedical applications.

Nowadays, some of the greatest challenges in the elaboration and use of nanoparticles or assemblies in biomedical applications concern achieving scalable and highly reproducible synthesis methods.[29–33] In this domain, microfluidics is a powerful strategy for the elaboration of inorganic building blocks and may be promising for their assembly into greater multifunctional hierarchical structures including into hybrid inorganic polymeric micelles.[34–38] Indeed, the better mixing provided in microfluidic systems due to their small scales compared to bulk methods, in addition due to the continuity of the flow, allow generation of large quantities of any nanostructure. When applied to the synthesis of polymeric micelles; assemblies can be formed through a process of nanoprecipitation in very short times and large scales.[39–41]

Herein, we report the use of a microfluidic-assisted method for the fast high-throughput and scalable assembly of magnetic micelles by the nanoprecipitation method for theranostic applications. We show the possibility to tune the morphology and size of the assemblies depending on the residence time conditions in the microfluidic system. Among the different assemblies, magnetomicelles with a diameter of roughly 49 nm were chosen as potential candidates for biomedical applications. Their optical properties and photothothermal functionalities in the biological window have been evaluated and compared to the bare iron oxide nanoflowers. We show that encapsulation in the micelle structure did not induce changes in their photothermal response. In addition, magnetic micelles can be used as negative contrast agents locally reducing the signal in MRI. Furthermore, we show that these particles rare biocompatible and have superior imaging tracer performance than that of commercial MPI contrast agents, such as Vivotrax® and Perimag®. Overall, our results demonstrate that the magnetic micelles can be considered as efficient multimodal nanoplatforms for theranostic applications.

Experimental

Chemicals & cells

All products listed are of analytical purity grade and they are used without further purification. Reagents and washing solvents are hydrochloric acid (HCl, 37%), nitric acid (HNO_3, 68%), ammonia (NH_3, 20%), ethanol (96%), acetone (>99%), diethyl ether (Et_2O, 100%), methanol (99.5%), all furnished by VWR International; trisodium citrate dihydrate ($C_6H_5Na_3O_7 \cdot 2H_2O$), oleic acid (>90%) and tetrahydrofuran anhydrous (THF, 99%) are supplied by Merck. The block copolymer polystyrene-*b*-poly(acrylic acid) (PS_{41000}-*b*-PAA_{4200}) is provided by Polymer Source, Inc (Canada). Microfluidic material is supplied by Cluzeau info labo (C.I.L., France) and consists of: a cross stainless-steel micromixer (10–32 for inner tubing 10/16″, 0.040″), Teflon PFA tubing (10/16″, 0.040″) and a PEEK tubing (360 μm × 150 μm, 0.006″). Human glioblastoma cells U87-MG (U87) were purchased from ATCC, Dulbecco's Modified Eagle's Medium (DMEM), heat inactivated foetal bovine serum (FBS) and penicillin-streptomycin were purchased from Life Technologies. Calcein-AM (≥95.0%) is purchased from Merk.

Synthesis of IONFs

The bulk synthesis of IONFs was performed using Fe(III) as the only precursor, as previously reported.[15] Hexahydrate ferric chloride (1.62 g, 6 mmol) was mixed in 80 mL of a mixture of DEG and NMDEA (1 : 1, v/v) until complete dissolution. In parallel, sodium hydroxide was dissolved in 40 mL of the same DEG/NMDEA mixture; the alkaline solution was added to the iron precursor solution under magnetic stirring 1 hour before raising the temperature. Lastly, 500 μL of MilliQ water was added to the reaction batch according to Hemery *et al.*[42] and the temperature was increased under reflux up to 220 °C. After cooling, the particles were magnetically separated and washed in HNO_3 (10%) to remove excess iron salts and confer to the NP surface a stabilizing positive charge; then twice with ethanol and acetone, before dispersing the final product in MilliQ water.

Surface modification of IONFs

The surface of IONFs was modified by grafting citric acid, to improve water-solubility, and oleic acid, to obtain a stable ferrofluid in aprotic polar solvents. In brief, tri-sodium citric acid salts were dissolved in the aqueous ferrofluid, in a mole ratio $n_{C_6H_5Na_3O_7}/n_{NP}^{Fe}$ equal to 0.13. The solution was heated to boil for 40 minutes and after cooling the product was washed thrice with acetone and twice with ethyl ether, before being dispersed in MilliQ water. Ammonia solution was added equimolarly to liquid oleic acid ($10 = n_{OA}/n_{NP}^{Fe}$) and magnetically stirred, in order to obtain a white thick mixture. At this point, also the IONF aqueous suspension was added and the solution was let stir for 10 minutes at room temperature. Afterwards, the temperature was raised to 50 °C for 30 min and the product was separated from the solvent by magnetic separation. It was also washed three times with 60 mL of methanol, and, after the last washing step, methanol was removed and a shiny precipitate was obtained; the final product was dispersed in

tetrahydrofuran anhydrous. The oleate-coated IONFs were used for the microfluidic synthesis of magnetic micelles, while citrated IONFs (for simplicity called later in the text IONFs) were used as a control in all experiments.

Microfluidic elaboration of magneto-micelles

Magnetomicelles were formed by nanoprecipitation: two solutions of PS-*b*-PAA (Mn = 41 000-*b*-4200, 1.8 g L^{-1}) and IONF@OAs (0.2 g L^{-1}) were mixed in a ratio of 4 : 1 v/v to prepare a stock solution that was ultrasonicated for some minutes before use. Three ECP2000 Analytical HPLC pumps (ECOM spol. s.r.o., Czech Republic) were connected to a stainless-steel cross junction: one central inlet was connected to the 150 μm PEEK tube and it was used for injecting the solution of block copolymer and IONFs in THF; two symmetrical inlets were used to pump MilliQ water. The outlet consisted of a flow focusing system, with water surrounding a THF focalised stream. Water and THF were pumped into the system in a 7 : 1 v/v ratio (α) at variable total flow rates (Q_{tot} = 0.4–22.8 mL min^{-1}). All syntheses were conducted in triplicate, to assess reproducibility. After synthesis, a mass of MilliQ water equal to half of the total mass of the fluid mixture was rapidly added to quench the growth of micelles and preserve the obtained conformation. The resulting solution was collected in a pear-shaped flask to eliminate THF through rotary evaporation (BUCHI rotavapor R-210, connected to a BUCHI vacuum pump V-700 and employing a BUCHI heating bath B-491). The micellar water suspension was filtered with a 0.45 μm Minisart® filter unit (Sartorius, Gottingen, Germany), it was let to precipitate on a permanent magnet and the pellet was collected and washed thrice with MilliQ water and subsequently stored at 4 °C.

Nanostructure's characterizations

The morphology of the NPs was imaged using a JEOL-1011 transmission electron microscope operating at 100 kV. Size distributions were determined using the opensource ImageJ software, manually measuring 300 NPs on at least three different images. The resulting histograms were modelled by a log-normal law using Igor Pro 7 software to determine the mean physical diameter (d_{TEM}) and the polydispersity (σ_{TEM}) of each sample. The total iron concentrations of NPs suspensions were measured by atomic absorption spectroscopy (AAS, PinAAcle 500, PerkinElmer) by degrading the samples in concentrated HCl (37%) before a dilution in HNO_3 (2%). Dynamic light scattering and zeta potential measurements were performed on a Malvern Zetasizer Nano-ZS. UV-Vis-NIR spectra (400–1100 nm) were recorded at room temperature in a 1 cm quartz cuvette using an Avantes spectrophotometric setup composed of an AvaLight-DHc lamp connected by optical fibers to a StarLine AvaSpec UV/Vis detector and to a NIRLine AvaSpec-NIR256-1.7 NIR detector. Aqueous suspensions were measured by VSM analysis in a static magnetic field comprised between −1 T and 1 T at 300 K.

Photothermia measurements

Infrared PT experiments were carried out using a 0.5 mL Eppendorf® containing 50 μL of the NP suspensions excited for 300 s by a NIR laser (808 nm or 1064 nm, power density = 0.28 W cm^{-2}) coupled to an optical fiber from Laser Components SAS (temperature increase is measured by an infrared camera FLIR SC7000. The specific loss power (SLP) variations as a function of total iron concentration was modelized according to:[43]

$$\mathrm{SLP}(\lambda) = \frac{P_0(\lambda)\cdot\eta(\lambda)}{m_{\mathrm{Fe}}}\cdot\left(1-10^{A(\lambda)}\right)$$

where $P_0(l)$ is the incident laser power (W cm^{-2}) at the excitation wavelength λ, $\eta(l)$ is the light-to heat conversion efficiency in photothermia at the excitation wavelength l, $A(\lambda)$ is the absorption at a given laser wavelength (λ) and is obtained by the Beer–Lambert law and m_{Fe} is the total mass of iron in the sample, expressed in g.

MRI measurements

MRI contrast agent performances of IONFs and IONFs@PS-*b*-PAA magnetomicelles were measured, in comparison with two different commercially available nanoparticles Perimag (Micromod GmbH, Germany) and Vivotrax (Magnetic Insight Inc, CA). The initial Fe concentrations of each sample were 25.4 mM for IONFs, 7.83 mM for IONFs@PS-*b*-PAA, 151.8 mM for Perimag, and 98.2 mM for Vivotrax. For each sample, dilution series with concentrations ranging between 0.01–0.5 mM Fe were prepared in doubly distilled water, with final volumes of 1.5 mL for each vial. T_1 and T_2 relaxation times of each dilution series were measured on a 3 T MRI scanner (Siemens Magnetom Trio) using a 32-channel head coil. For measuring r_1 relaxivity, an inversion recovery turbo spin echo sequence was utilized to acquire T_1-weighted images at 11 different inversion times (TI) ranging between 24–1900 ms. For measuring r_2 relaxivity, a single-echo spin echo sequence was utilized to acquire T_2-weighted images at 16 different echo times (TE) ranging between 8.5–1000 ms. The acquisition matrix sizes were 256 × 256 for T_1-weighted images and 128 × 102 for T_2-weighted images. Other imaging parameters for both sequences were TR = 2000 ms, 12 × 12 cm^2 field-of-view (FOV), and 4 mm slice thickness. To determine the T_1 and T_2 relaxation times at each concentration, MRI images were analyzed using an in-house MATLAB (Mathworks, Natick, MA) script. A fixed size region of interest (ROI) was drawn and placed over the relevant image region of each vial in the dilution series. T_1 was fitted using pixel intensities from T_1-weighted image ROIs of each vial as a function of TI, *via* a two-parameter signal recovery curve. T_2 was fitted using pixel intensities from T_2-weighted image ROIs of each vial as a function of TE, *via* a monoexponential signal decay curve. Finally, r_1 and r_2 relaxivities were determined *via* linear fitting to the inverses of T_1 and T_2 for the dilution series of each sample as functions of concentration, respectively, using the following relations:

$$\frac{1}{T_1} = \frac{1}{T_{1,0}} + r_1 C$$

$$\frac{1}{T_2} = \frac{1}{T_{2,0}} + r_2 C$$

Here, r_1 and r_2 are the relaxivities in mM^{-1} s^{-1}, C is the Fe concentration of each vial in the dilution series with the

corresponding T_1 and T_2 relaxation times, and $T_{1,0}$ and $T_{2,0}$ are the longitudinal and transverse relaxation times of the medium in the absence of contrast agents, respectively.

MPI measurements

MPI imaging tracer performances of the IONFs and IONFs@PS-*b*-PAA magnetomicelles were measured using an in-house magnetic particle spectroscopy (MPS) setup.[44] This setup measures the time-varying magnetization response of the IONPs under AC magnetic fields and is utilized to characterize MPI performance in terms of sensitivity and resolution capabilities. A sinusoidal drive field at 15 mT amplitude and 10 kHz frequency was applied to excite the sample, and the signal was received simultaneously *via* inductive signal reception. Undiluted samples were prepared in 0.2 mL PCR tubes. The initial Fe concentrations and volumes of each sample were 25.4 mM and 50 μL for IONFs, 7.83 mM and 125 μL for IONFs@PS-*b*-PAA, 151.8 mM and 50 μL for Perimag®, and 98.2 mM and 50 μL for Vivotrax®. The signal at the fundamental harmonic (*i.e.*, at 10 kHz) was discarded, and the signal at higher harmonics were utilized for evaluations. The MPI performances of the samples were then compared in terms of 5th-to-3rd harmonic ratio where higher values indicate improved resolution capability, and in terms of relative signal intensity normalized by Fe content where higher values indicate improved sensitivity capability.

Determination of aggregation parameter in DMEM

Samples were studied in water or DMEM supplemented with 2 mM citrate at room temperature using a backscattering angle of 173°. The aggregation percentage parameter δ_{agg} was calculated according to: $\delta_{agg} = (d_H - d_{TEM})/d_H$ where d_H is the hydrodynamic diameter and d_{TEM} the diameter deduced from TEM measurements.

Cell culture

Human glioblastoma cells U87-MG (U87, ATCC) were cultured at 37 °C and 5% CO_2 in DMEM, supplemented with 10% FBS and 1% penicillin-streptomycin. U87 were cultured on disposable 96-well plates at an initial seeding density of 25 000 cells per well. Cell viability was evaluated after 4 hours and overnight (~16 hours) incubation of NPs (0.05 mM, 0.1 mM, 0.25 mM, 0.5 mM, 0.75 mM and 1 mM) at 37 °C and 5% CO_2. When IONF@citrate were used, the culture medium was supplemented with additional citrate (2 mM) to maintain the colloidal stability. Once internalization was completed, cells were washed twice with phosphate buffered saline (PBS) solution and incubated for 1 hour with 100 μL of a solution of calcein-AM dye (3 μM) diluted in PBS. Fluorescence emission was then quantified by an automatic plate reader ($\lambda_{ex} = 494$ nm, $\lambda_{em} = 517$ nm).

Results & discussion

Tuning IONFs@PS-*b*-PAA assemblies and their scaling up by microfluidics

The continuous flow synthesis of IONF@PS-*b*-PAA magnetomicelles was achieved using a flow-focusing microfluidic system as schematized in Fig. 1. In this system, water was symmetrically injected from two inlets of a cross mixer with the same flow rate Q_1 and Q_2, while PS-*b*-PAA block copolymer and hydrophobic oleic acid coated IONFs dispersion in a THF solution was injected in the centre of the system (see Table S1† for exact flow rates). Water encircled the focalized stream of THF and the two fluids eventually mixed in the interdiffusion region of the system resulting in the self-assembly and encapsulation of IONFs and PS-*b*-PAA into a final magnetic micelle. Before inducing any self-assembly, we started by synthesizing the magnetic building block of the magnetomicelles. For this, magnetite IONFs were synthesized using the polyol process

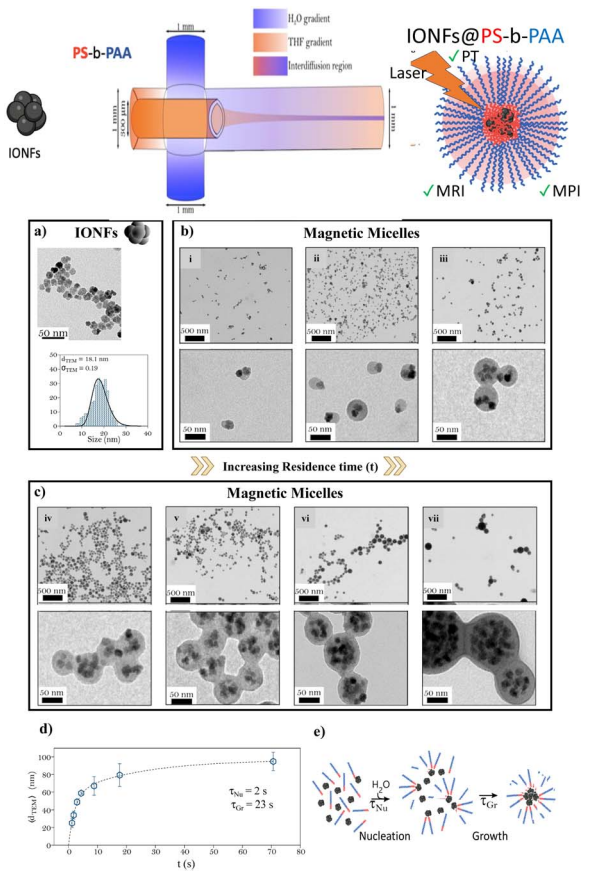

Fig. 1 Top scheme shows the microfluidic strategy used for the high-throughput synthesis of IONFs@PS-*b*-PAA polymeric magnetic micelles developed for photothermia (PTT), magnetic resonance imaging (MRI) and magnetic particle imaging (MPI). The two inlets of water and the outlet tubes of the flow focusing microreactor have an inner diameter of 1 mm, while the flow-focusing tube injecting the THF suspension has an inner diameter of 300 μm. Upon mixing by interdiffusion, self-assembly of IONFs and PS-*b*-PAA occurred resulting in the formation of final IONFS@PS-*b*-PAA magnetomicelles. (a) TEM image of magnetic iron oxide nanoflowers (IONFs) before encapsulation and its relative size distribution histogram. (b and c) TEM images of IONFs encapsulated in the polymeric micelles using different residence times during the microfluidic fabrication. (d) Evolution of the magnetomicelles average particle size $\langle d_{TEM} \rangle$ with residence time, error bars represent standard deviation. (e) Proposed two-step mechanism of magnetic micelles formation through nucleation (Nu) and growth (Gr) steps by nanoprecipitation in the microfluidic channel.

according to our previously established method,[15] followed by their surface modification with oleic acid for dispersion in THF. Fig. 1a shows the transmission electron microscopy (TEM) of the as-synthesized IONFS and their size distribution histogram fitted by a log normal law with an average diameter measured by TEM ($\langle d_{TEM} \rangle$) and corresponding polydispersity index ($\langle \sigma_{TEM} \rangle$). After this, we proceeded to the assembly of the IONFs and PS-*b*-PAA to form magnetomicelles. Considering the work of Wang *et al.*[45] on the synthesis of PS-*b*-PAA nanoparticles in a multiphase microfluidic reactor, where the authors associated the increase in the flow velocity of the solvent to the increase in nanoparticle size and shape transition from micelle to bicontinuous rods, we first studied the effect of variable total flow rates (Q_{tot}, Table S1†) and, consequently, residence times ($t = V/Q_{tot}$ where V is the volume of the channel, see Table S1†) on the final assemblies. The ratio of the flow rates of water/THF was kept at 7 which was found the best ratio for the formation of magnetomicelles based on a series of optimization. Fig. 1b and c depict the TEM images of the as synthetized magnetomicelles, and their corresponding experimental parameters are summarized in Table S1.† Assemblies of different shapes, including spherical, can be obtained depending on the flow conditions. For instance, at low residence times (Fig. 1b) one or two IONFs are asymmetrically embedded in a polymeric shell, in a conformation similar to a Janus particle. On the contrary, when the residence time increased, sphere-like shapes with the polymeric shell encircling almost the totality of IONFs were formed (Fig. 2c). The proposed explanation is that for low residence times, the velocity of the flow (and shear stress) is very high compared to the diffusion of the building blocks that leads to non-coalescence and assembly into non spherical shapes of the IONFs and the PS-*b*-PAA polymer.

We evaluated the size distribution for the magnetic micelles obtained in each experimental condition (Fig. S1 and Table S2†), extracting the average diameter $\langle d_{TEM} \rangle$ and polydispersity $\langle \sigma_{TEM} \rangle$, respectively. They show that magnetic assemblies with a size ranging from 25 to 95 nm can be easily prepared by simply tuning the residence time from 1 to 71 s. In all cases high-throughput elaboration and scaling up was achieved due to the high total flow rates (up to 22.857 mL min^{-1}, as shown in Table S1†), which is a considerable improvement when compared to the previously reported addition times of 10 μL min^{-1} for bulk syntheses.[28] Finally, the evolution of magnetic micelle's size with residence time is shown in Fig. 1d. It was fitted to a double exponential profile with two characteristic times. Considering an order of magnitude of solvent diffusivities (D) of about 5×10^{-9} m^2 s^{-1} and a mixing distance (w) of 300 μm, a mixing time $t_{mix} = w^2/2D = 9$ s was calculated. We propose that the two characteristic times in Fig. 1d might be related to the nucleation ($\tau_{Nu} = 2$ s) and growth ($\tau_{Gr} = 23$ s) of the micelles, respectively, as schematized in Fig. 1e. This mechanism of formation is in good agreement with other propositions found in the literature for polymeric micelles.[30] The zeta potential of citrated IONFs and IONFs@PS-*b*-PAA assemblies and their relative hydrodynamic diameter (d_H) were measured at pH = 7 in water. Citrated IONFs showed a value around −47 (±9) mV and d_H of 35 ± 3 nm. In the case of the magnetomicelles d_H increased from 26 (sample i) to 228 nm (sample vii) depending on the flow conditions in agreement with the changes observed by TEM and the aggregation parameter while an average zeta potential around 27 ± 4 mV was observed for all magnetomicelles. These values agreed well with the previously reported values on IONFs and other PAA-coated NPs.[46,47]

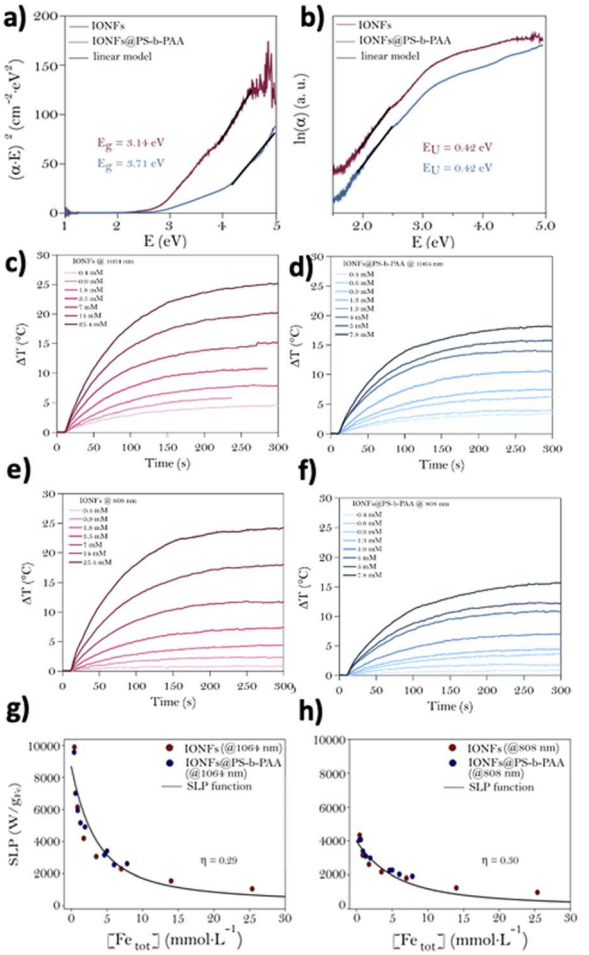

Fig. 2 Characterization of the optical properties and photothermal function of IONFs and IONFs@PS-*b*-PAA magnetomicelles. Determination from UV-Vis-NIR extinction spectra of the gap energy (E_g) using (a) Tauc plots and (b) Urbach energy (E_U) using Urbach plots. Temperature elevation as a function of exposure time after irradiation at a surface power density of 0.3 W cm^{-2} with a 1064 nm laser of (c) IONFs (c) or (d) magnetic micelles, or after irradiation with an 808 nm laser source of (e) IONFs or (f) magnetic micelles; measured SLP values as a function of total iron concentration for (g) IONFs and (h) IONFs@PS-*b*-PAA when exposed to a 1064 nm and 808 nm laser source (0.3 W cm^{-2}), black line: SLP fit function.

Magnetomicelles are efficient in photothermia

After their synthesis and physico-chemical characterization, the 49 nm diameter IONFs@PS-*b*-PAA magnetic assemblies were chosen as candidates for the rest of the work, motivated by their size compatible for theranostic applications. The first step was then to investigate the impact of PS-*b*-PAA on the optical

properties and photothermal performance of the encapsulated IONFs. UV-Vis-NIR extinction spectra of citrate-modified IONFs and IONFs@PS-*b*-PAA magnetic micelles are shown in Fig. S2a and b,† respectively. Both displayed the typical spectral profile of magnetite with an increasing absorption towards 1100 nm as a signature of the intervalence band (IVCT) of magnetite. The molar extinction coefficients extracted from these Beer–Lambert plots at 1064 nm and 808 nm ($\varepsilon_{1064\ nm}$ and $\varepsilon_{808\ nm}$) are shown in Fig. S3a and b.† It shows higher extinction coefficients at 1064 nm compared to 808 nm for both free and encapsulated IONFs, in agreement with the presence of the IVCT band. After encapsulation of the IONFs in the PS-*b*-PAA shell, ε increased respectively from 47 to 89 L mol_{Fe}^{-1} cm^{-1} at 808 nm and from 89 to 126 L mol_{Fe}^{-1} cm^{-1} at 1064 nm. These values of the free IONFs were in good agreement with previously reported results.[15]

To understand the origin of ε increase after encapsulation, optical simulations were carried out, based on Mie theory and using the Mie Python module developed by S. Prahl.[48] The refractive indexes of Fe_3O_4 (Table S3†) and PS (Table S4†) allowed to obtain the cross-section profile of extinction, absorption and scattering of NPs (Fig. S4†). As shown, the extinction profile of magnetite nanoparticles assumed with a diameter of 49 nm was mainly dominated by absorption, while the scattering contribution was neglectable. The situation was reversed in the case of a PS nanoparticle of 49 nm diameter, showing a scattering-dominated extinction profile (Fig. S4b†). In addition, at 808 nm and 1064 nm wavelengths the absorption of a hypothetical 49 nm diameter IONF (mainly due to absorption) was approximately 1000 times higher than the scattering of the 49 nm PS NP. Consequently, the increase in $\varepsilon_{1064\ nm}$ and $\varepsilon_{808\ nm}$ after the encapsulation of Fe_3O_4 NFs in the polymeric micelle may be explained by the increased number of IONFs. Encapsulation of IONFs in a polymeric shell may induce changes in the gap energy of the nanoparticles and induce defects with direct consequences on the final optical properties and photothermal activity.[49] Consequently, the extinction spectra were used, as described elsewhere,[15,50] for the determination of both the gap energy (E_g) from Tauc plots and Urbach Energy (E_U), as the latter directly translates the presence of defects in the nanoparticles (Fig. 2a and b, respectively). Band gap energies of 3.14 and 3.71 eV for the free and encapsulated IONFs, respectively, were extracted demonstrating an impact of encapsulation on IONFs. Such shift toward high energies can be explained by the presence of the organic polymer shell with high absorption in the UV area. However, the values of E_g were of the same order of magnitude of those available in literature for magnetic iron oxides *i.e.* 3.42 eV.[50,51] At the same time, E_U values of magnetite samples before and after encapsulation showed a similar value of 0.42 eV, in good agreement with those obtained elsewhere for bare Fe_3O_4 IONFs,[15] establishing that neither their surface modification with oleic acid nor their encapsulation with the polymeric shell create defects in the NPs.

Next, considering the potential use of these magnetic micelles in the realm of nanomedicine for photothermal applications, we evaluated the photothermal conversion efficiencies of the nanomaterials. The heating produced by the IONFs before and after encapsulation in the PS-*b*-PAA micelles was assessed by measuring the increase in temperature (for similar iron concentration) under the excitation of 1064 nm or 808 nm laser excitations, both with a power density of 0.3 W cm^{-2} (Fig. 2c–f). This power density was chosen since it represents the safe conditions for the surrounding healthy tissues if photothermal therapy is applied *in vivo*. When excited with 1064 nm, high ΔT of about 25 °C was achieved with the IONFs at [Fe] = 25.4 mM in good agreement with previous reports. Concentrations over 10 mM of Fe are not likely to be reached *in vivo*. ΔT values around 15 °C can be still reached for both IONFs ([Fe] = 7 mM) and IONFs@PS-*b*-PAA ([Fe] = 7.8 mM), when excited at 1064 nm showing that encapsulation has little impact on PT at such concentrations. For all nanostructures and Fe concentrations tested, heat generation under 1064 nm irradiation showed a slight increase of ΔT by ≈ 1–1.5 °C compared to the 808 nm laser, which was attributed to the presence of the IVCT. Specific loss power (SLP) of all samples was evaluated with both laser sources (1064 nm and 808 nm) and at a biosafe surface power density of 0.3 W cm^{-2}. SLP values (obtained from the heating curves shown in Fig. 2) are reported as a function of Fe sample concentration. The parameter light-to-heat conversion (η) was obtained for all sets of samples: it appears that light was converted efficiently to heat and in the same way for free or encapsulated Fe_3O_4 samples ($\eta \approx 30\%$) in the explored NIR region of interest for biomedical applications. Higher SLP values were reached at a similar Fe concentration when the 1064 nm source was used rather than 808 nm, (7000 W g^{-1} Fe and 3600 W g^{-1} Fe, respectively, for [Fe] = 1 mM) as shown in Fig. 2g and h). Therefore, these results indicate that the encapsulation of IONFs in the polymeric shell has no impact on their heating function.

Magnetomicelles as dual MRI and MPI imaging agents

In MRI, IONPs are widely used as contrast agents for applications such as liver imaging, inflammation imaging, and cell tracking.[52] IONPs are classified as either positive contrast agents that locally increase the MRI signal by shortening the longitudinal relaxation time (T_1), or as negative contrast agents that locally decrease the MRI signal by shortening the transverse relaxation time (T_2). The performance of a contrast agent is determined *via* its longitudinal relaxivity (r_1) and transverse relaxivity (r_2), with larger relaxivities indicating higher positive contrast and negative contrast capabilities, respectively. Magnetic particle imaging (MPI) is a rapidly developing tracer-based imaging modality that images the spatial distribution of IONPs *in vivo*, with applications such as cancer imaging, cell tracking, and inflammation imaging.[53] The image quality in MPI is highly dependent on the properties of the IONPs, which prompted numerous research groups to synthesize tracers tailored specifically for MPI, demonstrating improved sensitivity and resolution when compared to IONPs designed for use in MRI.[54,55] Fig. 3 shows the MRI and MPI performances of the IONFs and IONFs@PS-*b*-PAA, in comparison with commercially available Perimag® and Vivotrax® nanoparticles. Fig. 3a and b shows example T_1-weighted and T_2-weighted MRI images, respectively, depicting different pixel intensities at different Fe concentrations. Fig. 3b shows r_1

and r_2 relaxivity curves for each sample, with numeric values provided in Fig. 3f. Higher relaxivities indicate improved MRI contrast agent performance. Accordingly, for all nanoparticles, r_2 relaxivities are considerably large and r_1 relaxivities are relatively small, indicating that these nanoparticles can be classified as T_2-agents or negative contrast agents to locally reduce the signal in MRI.[56] Both IONFs and IONFs@PS-*b*-PAA have significantly larger r_2 relaxivities when compared to commercial samples Perimag® and Vivotrax®, indicating superior MRI performance as negative contrast agents. The relatively reduced r_2 relaxivity of IONFs@PS-*b*-PAA when compared to that of IONFs may be attributed to the fact that nanoflowers are encapsulated in polystyrene core of the micelles, reducing their access to the surrounding water molecules. Fig. 3e shows MPI performance of the tested samples, plotting the normalized signal amplitude as a function of harmonics. Fig. 3f shows a list of the MPI performance metrics for the tested samples. Slower signal decay at higher harmonics (*i.e.*, high 5th-to-3rd harmonic ratio) indicates good MPI resolution performance, and high signal intensity per Fe content indicates signal efficiency, implying that a reduced dose can be utilized to achieve the same signal in the case of high signal efficiency. Accordingly, Perimag® has the highest 5th-to-3rd harmonic ratio, together with the highest relative signal, indicating superior performance in terms of both resolution and signal intensity. Note that this result is to be expected, as Perimag® was custom designed for increased performance in MPI.[57] IONFs@PS-*b*-PAA has the second-best performance in terms of both 5th-to-3rd harmonic ratio and relative signal. While IONFs nanoparticles have significantly higher relative signal than Vivotrax®, their 5th-to-3rd harmonic ratios are similar. This latter result implies that a larger portion of the nanoparticles that make up IONFs contribute to the MPI signal (*e.g.*, Vivotrax® may contain very small IONPs that do not contribute to the signal but contribute to the Fe content, thereby reducing its signal efficiency). The differences between the IONFs and IONFs@PS-*b*-PAA can be attributed to the potential differences in magnetic interactions among the IONFs in these two cases. Accordingly, the interactions for IONFs@PS-*b*-PAA enhanced its MPI imaging tracer performance over that for IONFs.

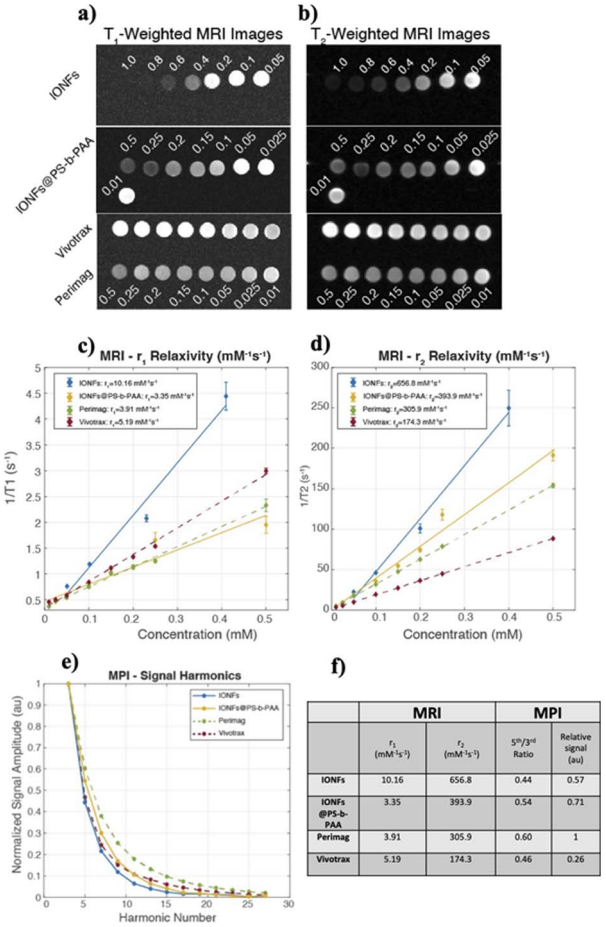

	MRI		MPI	
	r_1 ($mM^{-1}s^{-1}$)	r_2 ($mM^{-1}s^{-1}$)	$5^{th}/3^{rd}$ Ratio	Relative signal (au)
IONFs	10.16	656.8	0.44	0.57
IONFs @PS-b-PAA	3.35	393.9	0.54	0.71
Perimag	3.91	305.9	0.60	1
Vivotrax	5.19	174.3	0.46	0.26

Fig. 3 MRI and MPI performances for IONFs and IONFs@PS-*b*-PAA magnetomicelles. Commercially available Perimag® and Vivotrax® nanoparticles are used for comparison. Example (a) T_1-weighted and (b) T_2-weighted MRI images for the samples. MRI contrast agent performances measured *via* (c) r_1 and (d) r_2 relaxivities. The inverses of T_1 and T_2 relaxation time constants are plotted as a function of concentration, with the slopes corresponding to r_1 and r_2 relaxivities. (e) MPI performances compared *via* normalized signal amplitude plotted as a function of harmonic number. (f) MRI and MPI performances quantified in terms of r_1 and r_2 relaxivities for MRI, and 5th-to-3rd harmonic ratio and relative signal intensity normalized by Fe content for MPI.

It has been shown in the literature that nanoparticles with core diameter smaller than 10 nm do not contribute to the MPI signal, whereas those larger than 20 nm exhibit dramatically slow relaxations that inhibit their MPI signal.[58] Furthermore, nanoparticles larger 20 nm may no longer exhibit superparamagnetism, a requirement for MRI contrast capability.[59] The core diameter distribution of IONFs shown in Fig. 1a falls within this critical range of diameters, granting them simultaneous MPI and MRI contrast capability. When compared to nanoparticles presented in the literature, IONFs have core diameter comparable to that of Prerimag® and slightly smaller than that of Resovist®.[57] Previous work has shown that introducing selective zinc doping can help improve both the MPI and magnetic heating performances of nanoparticles.[60] Another work has shown that co-encapsulation iron oxide with hafnium oxide can enable dual MPI and computed tomography (CT) contrast capability.[61] The iron oxide nanoparticles in the latter study had comparable core diameters to that of IONFs in our work, but co-encapsulation with hafnium oxide caused a reduction in their core diameter, with a drawback of reduction in MPI resolution capability. While the effects of such doping or co-encapsulation processes were not shown for MRI or photothermia, they may also benefit IONFs presented in this work, further widening their application areas.

Assessing the biocompatibility of the magnetomicelles

Prior to testing the biocompatibility of the magnetic micelles, dynamic light scattering (DLS) analysis was used to verify the colloidal stability of the samples in cell culture medium. Fig. S5† shows the evolution of a parameter of aggregation (δ_{agg}), expressed as a percentage, during 4 hours after the addition of

the NPs to complete DMEM. The sample hydrodynamic size was measured every 15 minutes at 37 °C. Compared to the citrated IONFs, where complete aggregation (over 90%) was observed (as well as sedimentation due to the formation of big aggregates), the magnetic micelles displayed only ~50% aggregation and no tendency for precipitation, showing that encapsulation of IONFs in the polymeric micelles improves their stability and therefore validating their potential in nanomedicine. Next, to identify the best-suited conditions of incubation while preserving the cellular viability, calcein-AM viability assays were performed on U87 cells at different iron doses (0.05 mmol L^{-1}, 0.1 mmol L^{-1}, 0.25 mmol L^{-1}, 0.5 mmol L^{-1}, 0.75 mmol L^{-1} and 1 mmol L^{-1}) and incubation times (4 hours and 24 hours). Fig. 4 shows the relative viability of U87 cells after being incubated with IONFs or magnetic micelles for either 4 h or overnight. Cell viability did not reduce further than 75% even at the highest concentration of IONFs, for both incubation periods (Fig. 4a and c), which is in good agreement with the well-known biocompatibility of citrate-coated iron oxides documented in literature.[62] On the contrary, a 4 hours incubation of U87 cells with magnetic micelles led to a dose-dependent viability loss (Fig. 4b). A similar, but less defined tendency was observed after overnight incubation of magnetomicelles (Fig. 4d). This dose-dependent viability loss, which was not observed for IONFs, could be due to effects of the polymer on cell viability or to the increase in NP size. Despite this, both IONFs and magnetic micelles show good biocompatibility which enables their potential as theranostics agents, as they are biocompatible at concentrations with good MPI and MRI signals.

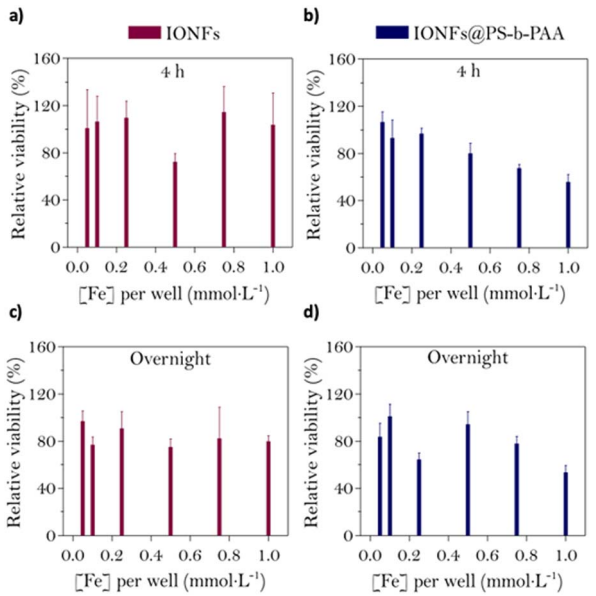

Fig. 4 Relative cell viability, expressed as a percentage, as a function of iron initial dose (0.05 mmol L^{-1}, 0.1 mmol L^{-1}, 0.25 mmol L^{-1}, 0.5 mmol L^{-1}, 0.75 mmol L^{-1} and 1 mmol L^{-1}) for IONFs after (a) 4 hours and (c) overnight incubation with U87 cells; and for IONFs@PS-*b*-PAA magnetomicelles after (b) 4 hours and (d) overnight incubation with U87 cells. All tests are conducted in triplicate and error bars stand for standard deviations.

Conclusions

In summary, we have successfully demonstrated a novel high-throughput microfluidic-assisted method to fabricate magnetomicelles based on a IONFs multicores and a PS-*b*-PAA. We showed that by modulating the residence time in the microfluidic channel, we could control the size and shape of the magnetomicelles. Furthermore, we gained insights into the nucleation and growth processes of the formation of magnetomicelles at a fundamental level. Envisioning potential applications of these magnetomicelles as theranostic agents, we evaluated their performance in photothermia. Interestingly, we showed that despite having the IONFs encapsulated in the polymer the light-to-heat conversion remained unaffected. In addition, we explored the imaging functionalities of these nanohybrids for magnetic imaging techniques such as MRI and MPI and compared their performance with the bare IONFs and two commercially available particles. We showed that both IONFs and magnetomicelles hold promise as negative contrast agents for MRI, and that the magnetomicelles performed exceptionally well as imaging tracers in MPI. To further validate the applicability of the magnetomicelles in theranostics, we confirmed their biocompatibility by incubating them with a glioblastoma cell line, demonstrating that they are biocompatible. Altogether, these results underscore the potential of magnetomicelles are great candidates to explore as multimodal nanotheranostic agents, particularly as photothermal and imaging contrast agents. Having established the properties and multifunctionality of these nanohybrid magnetomicelles, our future research aims to investigate the impact of biological processing on their structure and theranostic performances.

Conflicts of interest

There are no conflicts to declare.

Acknowledgements

E. B. and A. A.-H acknowledge the support of the French Agence Nationale de la Recherche (ANR), under grant ANR-18-CE09-0004 (project MicroNanoCell). A. A.-H. and C. W. acknowledge the support of the French Agence Nationale de la Recherche (ANR), under grant ANR-19-CE09-0029 (project SuperMagStemCells).

Notes and references

1 S. K. Avugadda, S. Wickramasinghe, D. Niculaes, M. Ju, A. Lak, N. Silvestri, S. Nitti, I. Roy, A. C. S. Samia and T. Pellegrino, *Nanomaterials*, 2021, **11**, 62.
2 J. Kolosnjaj-Tabi, L. Lartigue, Y. Javed, N. Luciani, T. Pellegrino, C. Wilhelm, D. Alloyeau and F. Gazeau, *Nano Today*, 2016, **11**, 280–284.
3 H. Gavilán, S. K. Avugadda, T. Fernández-Cabada, N. Soni, M. Cassani, B. T. Mai, R. Chantrell and T. Pellegrino, *Chem. Soc. Rev.*, 2021, **50**, 11614–11667.

4 W. Xie, Z. Guo, F. Gao, Q. Gao, D. Wang, B.-S. Liaw, Q. Cai, X. Sun, X. Wang and L. Zhao, *Theranostics*, 2018, **8**, 3284–3307.
5 B. Chertok, B. A. Moffat, A. E. David, F. Yu, C. Bergemann, B. D. Ross and V. C. Yang, *Biomaterials*, 2008, **29**, 487–496.
6 B. Freis, M. L. A. Ramirez, C. Kiefer, S. Harlepp, C. Iacovita, C. Henoumont, C. Affolter-Zbaraszczuk, F. Meyer, D. Mertz, A. Boos, M. Tasso, S. Furgiuele, F. Journe, S. Saussez, S. Bégin-Colin and S. Laurent, *Pharmaceutics*, 2023, **15**, 1104.
7 J. Kolosnjaj-Tabi, C. Wilhelm, O. Clément and F. Gazeau, *J. Nanobiotechnol.*, 2013, **11**, S7.
8 C. Rigoni, J. Fresnais, D. Talbot, R. Massart, R. Perzynski, J. C. Bacri and A. Abou-Hassan, *Langmuir*, 2020, **36**, 5048–5057.
9 Y. Fernández-Afonso, L. Asín, L. Beola, R. M. Fratila and L. Gutiérrez, *ACS Appl. Nano Mater.*, 2022, **5**, 16220–16230.
10 S. Shaw, J. Kailashiya, A. Gangwar, S. Alla, S. K. Gupta, C. Prajapat, S. S. Meena, D. Dash, P. h. Maiti and N. Prasad, *Appl. Surf. Sci.*, 2021, **560**, 150025.
11 C.-C. Huang, P.-Y. Chang, C.-L. Liu, J.-P. Xu, S.-P. Wu and W.-C. Kuo, *Nanoscale*, 2015, **7**, 12689–12697.
12 S. Cabana, A. Curcio, A. Michel, C. Wilhelm and A. Abou-Hassan, *Nanomaterials*, 2020, **10**, 1548.
13 E. Cazares-Cortes, S. Cabana, C. Boitard, E. Nehlig, N. Griffete, J. Fresnais, C. Wilhelm, A. Abou-Hassan and C. Ménager, *Adv. Drug Delivery Rev.*, 2019, **138**, 233–246.
14 A. Espinosa, J. Kolosnjaj-Tabi, A. Abou-Hassan, A. Plan Sangnier, A. Curcio, A. K. A. Silva, R. Di Corato, S. Neveu, T. Pellegrino, L. M. Liz-Marzán and C. Wilhelm, *Adv. Funct. Mater.*, 2018, **28**, 1803660.
15 E. Bertuit, E. Benassai, G. Mériguet, J.-M. Greneche, B. Baptiste, S. Neveu, C. Wilhelm and A. Abou-Hassan, *ACS Nano*, 2022, **16**, 271–284.
16 E. Bertuit, N. Menguy, C. Wilhelm, A.-L. Rollet and A. Abou-Hassan, *Commun. Chem.*, 2022, **5**, 164.
17 Y. Mai and A. Eisenberg, *Chem. Soc. Rev.*, 2012, **41**, 5969–5985.
18 M. J. Robb, L. A. Connal, B. F. Lee, N. A. Lynd and C. J. Hawker, *Polym. Chem.*, 2012, **3**, 1618–1628.
19 N. Liu, L. Wu, W. Zuo, Q. Lin, J. Liu, Q. Jin, Z. Xiao, L. Chen, Y. Zhao, J. Zhou and X. Zhu, *ACS Appl. Mater. Interfaces*, 2022, **14**, 29668–29678.
20 S. Lecommandoux, O. Sandre, F. Chécot, J. Rodriguez-Hernandez and R. Perzynski, *J. Magn. Magn. Mater.*, 2006, **300**, 71–74.
21 J.-F. Berret, N. Schonbeck, F. Gazeau, D. El Kharrat, O. Sandre, A. Vacher and M. Airiau, *J. Am. Chem. Soc.*, 2006, **128**, 1755–1761.
22 J. Wang, W. Li and J. Zhu, *Polymer*, 2014, **55**, 1079–1096.
23 L. Zhang and A. Eisenberg, *J. Am. Chem. Soc.*, 1996, **118**, 3168–3181.
24 Q. Chen, H. Schönherr and G. J. Vancso, *Small*, 2010, **6**, 2762–2768.
25 M. Zatorska-Płachta, G. Łazarski, U. Maziarz, A. Foryś, B. Trzebicka, D. Wnuk, K. Chołuj, A. Karewicz, M. Michalik, D. Jamróz and M. Kepczynski, *ACS Omega*, 2021, **6**, 12168–12178.
26 B. H. Vilsinski, M. A. Witt, P. M. Barbosa, M. C. Montanha, C. S. Nunes, I. C. Bellettini, L. V. de Castro, F. Sato, M. L. Baesso, E. C. Muniz and W. Caetano, *J. Mol. Liq.*, 2018, **271**, 949–958.
27 B.-S. Kim, J.-M. Qiu, J.-P. Wang and T. A. Taton, *Nano Lett.*, 2005, **5**, 1987–1991.
28 R. J. Hickey, A. S. Haynes, J. M. Kikkawa and S.-J. Park, *J. Am. Chem. Soc.*, 2011, **133**, 1517–1525.
29 P. L. Saldanha, V. Lesnyak and L. Manna, *Nano Today*, 2017, **12**, 46–63.
30 R. Karnik, F. Gu, P. Basto, C. Cannizzaro, L. Dean, W. Kyei-Manu, R. Langer and O. C. Farokhzad, *Nano Lett.*, 2008, **8**, 2906–2912.
31 H. Gavilán, G. M. R. Rizzo, N. Silvestri, B. T. Mai and T. Pellegrino, *Nat. Protoc.*, 2023, **18**, 783–809.
32 S. Falsini, U. Bardi, A. Abou-Hassan and S. Ristori, *Green Chem.*, 2018, **20**, 3897–3907.
33 R. A. Petros and J. M. DeSimone, *Nat. Rev. Drug Discovery*, 2010, **9**, 615–627.
34 Q. Feng, J. Sun and X. Jiang, *Nanoscale*, 2016, **8**, 12430–12443.
35 L. Wang and J. Wang, *Nanoscale*, 2019, **11**, 16708–16722.
36 J. Ma, S. M.-Y. Lee, C. Yi and C.-W. Li, *Lab Chip*, 2017, **17**, 209–226.
37 J. Schemberg, A. E. Abbassi, A. Lindenbauer, L.-Y. Chen, A. Grodrian, X. Nakos, G. Apte, N. Khan, A. Kraupner, T.-H. Nguyen and G. Gastrock, *ACS Appl. Mater. Interfaces*, 2022, **14**, 48011–48028.
38 M. O. Besenhard, L. Storozhuk, A. P. LaGrow, L. Panariello, A. Maney, S. Pal, C. Kiefer, D. Mertz, L. D. Tung, M. R. Lees, N. T. K. Thanh and A. Gavriilidis, *Chem. Eng. J.*, 2023, 144542, DOI: **10.1016/j.cej.2023.144542**.
39 L. Capretto, D. Carugo, S. Mazzitelli, C. Nastruzzi and X. Zhang, *Adv. Drug Delivery Rev.*, 2013, **65**, 1496–1532.
40 L. Capretto, D. Carugo, W. Cheng, M. Hill and X. Zhang, *J. Colloid Interface Sci.*, 2011, **357**, 243–251.
41 D. Habault, A. Dery, J. Leng, S. Lecommandoux, J. F. L. Meins and O. Sandre, *IEEE Trans. Magn.*, 2013, **49**, 182–190.
42 G. Hemery, A. C. Keyes, E. Garaio, I. Rodrigo, J. A. Garcia, F. Plazaola, E. Garanger and O. Sandre, *Inorg. Chem.*, 2017, **56**, 8232–8243.
43 K. Jiang, D. A. Smith and A. Pinchuk, *J. Phys. Chem. C*, 2013, **117**, 27073–27080.
44 A. Alpman, M. Utkur and E. Ulku saritas, *J. Magn. Part. Imaging*, 2022, **8**, 2203013.
45 C.-W. Wang, D. Sinton and M. G. Moffitt, *J. Am. Chem. Soc.*, 2011, **133**, 18853–18864.
46 B. Liu, Y. Chen, C. Li, F. He, Z. Hou, S. Huang, H. Zhu, X. Chen and J. Lin, *Adv. Funct. Mater.*, 2015, **25**, 4717–4729.
47 S. H. Brewer, W. R. Glomm, M. C. Johnson, M. K. Knag and S. Franzen, *Langmuir*, 2005, **21**, 9303–9307.
48 S. Prahl, **https://github.com/scottprahl/miepython**.
49 S. Nemec, S. Kralj, C. Wilhelm, A. Abou-Hassan, M.-P. Rols and J. Kolosnjaj-Tabi, *Appl. Sci.*, 2020, **10**, 7322.
50 M. E. Sadat, M. K. Baghbador, A. W. Dunn, H. P. Wagner, R. C. Ewing, J. Zhang, H. Xu, G. M. Pauletti, D. B. Mast and D. Shi, *Appl. Phys. Lett.*, 2014, **105**, 091903.

51 W. Fontijn, P. Van der Zaag, M. Devillers, V. Brabers and R. Metselaar, *Phys. Rev. B*, 1997, **56**, 5432.
52 J. W. M. Bulte and D. L. Kraitchman, *NMR Biomed.*, 2004, **17**, 484–499.
53 E. U. Saritas, P. W. Goodwill, L. R. Croft, J. J. Konkle, K. Lu, B. Zheng and S. M. Conolly, *J. Magn. Reson.*, 2013, **229**, 116–126.
54 L. W. E. Starmans, D. Burdinski, N. P. M. Haex, R. P. M. Moonen, G. J. Strijkers, K. Nicolay and H. Grüll, *PLoS One*, 2013, **8**, e57335.
55 R. M. Ferguson, A. P. Khandhar, S. J. Kemp, H. Arami, E. U. Saritas, L. R. Croft, J. Konkle, P. W. Goodwill, A. Halkola, J. Rahmer, J. Borgert, S. M. Conolly and K. M. Krishnan, *IEEE Trans. Med. Imaging*, 2015, **34**, 1077–1084.
56 D.-B. Shieh, F.-Y. Cheng, C.-H. Su, C.-S. Yeh, M.-T. Wu, Y.-N. Wu, C.-Y. Tsai, C.-L. Wu, D.-H. Chen and C.-H. Chou, *Biomaterials*, 2005, **26**, 7183–7191.
57 D. Eberbeck, C. L. Dennis, N. F. Huls, K. L. Krycka, C. Gruttner and F. Westphal, *IEEE Trans. Magn.*, 2013, **49**, 269–274.
58 R. M. Ferguson, K. R. Minard, A. P. Khandhar and K. M. Krishnan, *Med. Phys.*, 2011, **38**, 1619–1626.
59 L. Li, W. Jiang, K. Luo, H. Song, F. Lan, Y. Wu and Z. Gu, *Theranostics*, 2013, **3**, 595–615.
60 L. M. Bauer, S. F. Situ, M. A. Griswold and A. C. S. Samia, *Nanoscale*, 2016, **8**, 12162–12169.
61 S. Liu, A. Heshmat, J. Andrew, I. Barreto and C. M. Rinaldi-Ramos, *Nanoscale Adv.*, 2023, **5**, 3018–3032.
62 E. Carenza, V. Barceló, A. Morancho, J. Montaner, A. Rosell and A. Roig, *Acta Biomater.*, 2014, **10**, 3775–3785.